Journal of Ocean Engineering and Marine Energy (2018) 4:243–257
https://doi.org/10.1007/s40722-018-0119-9

RESEARCH ARTICLE

Experimental investigation of nonlinear internal waves in deep water with miscible fluids

R. Camassa[1] · M. W. Hurley[1] · R. M. McLaughlin[1] · P.-Y. Passaggia[2] · C. F. C. Thomson[1]

Received: 19 May 2018 / Accepted: 22 August 2018 / Published online: 7 September 2018

Abstract
Laboratory experimental results are presented for nonlinear internal solitary waves (ISW) propagation in 'deep water' configuration with miscible fluids. The results are validated against direct numerical simulations and traveling wave exact solutions where the effect of the diffused interface is taken into account. The waves are generated by means of a dam break and their evolution is recorded with laser-induced fluorescence and particle image velocimetry. In particular, data collected in a frame moving with the waves are presented here for the first time. Our results are representative of geophysical applications in the deep ocean where weakly nonlinear theories fail to capture the characteristics of large amplitude ISWs from field observations.

Keywords Solitary waves · Nonlinear waves · Internal waves · Deep water · Experimental methods

1 Introduction

Diurnal and semi-diurnal ocean tides generate large-amplitude ISWs, as observed for instance on the Hawaiian ridge (Rudnick et al. 2003), near the Luzon strait (Duda et al. 2004; Alford et al. 2015), in the gulf of Alaska (Churnside and Ostrovsky 2005), in the Sulu sea (Apel et al. 1985), off the coast of California (Pinkel 1979), and more recently in the Tasman sea (Johnston et al. 2015), and the Washington Shelf (Zhang and Alford 2015). These large-amplitude ISWs propagate for very long distances from their sources (Hosegood and van Haren 2006; Simmons and Alford 2012) across the deep ocean (see Helfrich and Melville 2006 for a review on ISWs), have been observed to reach amplitudes as large as 300 m (Rudnick et al. 2003) or with nonlinearity $\alpha = \eta_{\max}/h \approx 5$, where h is an appropriate reference depth scale (Stanton and Ostrovsky 1998). Such large-amplitude internal solitary waves induce localized regions of strong shear flows that contribute to a large amount of mixing near the bottom (van Haren 2013) and across the thermocline (Liu et al. 1985; Brandt et al. 2002). Internal solitary waves are also likely to be amplified by interaction with mesoscale eddies (Xie et al. 2015). ISWs play a central role in ocean circulation as they provide a means for mixing and dissipation in the pycnocline of both the deep ocean (Grimshaw et al. 2003; Grimshaw and Helfrich 2012) and the continental shelf (Lamb 2014; Alford et al. 2015; Bourgault et al. 2016; Passaggia et al. 2018).

While the dynamics of ISWs in shallow configurations has arguably received most of the attention in the literature (see, e.g., Helfrich and Melville 2006 for a review, and Zhao et al. 2016 for very recent developments) its deep water counterpart has been extensively studied mainly from a mathematical perspective, and this mostly in the weakly nonlinear and two-layer regimes modelled by, respectively, the Korteweg-de-Vries (KdV) (Grimshaw 1981), the intermediate long

RC, RMM, and CT acknowledge the support by the National Science Foundation under grants RTG DMS-0943851, CMG ARC-1025523, DMS-1009750, DMS-1517879, and DURIP N00014-12-1-0749. PYP acknowledges the support by the National Science Foundation under grant NSF OCE-1155558 and NSF OCE-1736989.

✉ P.-Y. Passaggia
passaggia@unc.edu

R. Camassa
camassa@amath.unc.edu

M. W. Hurley
hurleymatthew1@gmail.com

R. M. McLaughlin
rmm@email.unc.edu

C. F. C. Thomson
cfct@email.unc.edu

[1] Department of Mathematics, Carolina Center for Interdisciplinary Applied Mathematics, University of North Carolina, Chapel Hill, NC 27599, USA

[2] Department of Marine Sciences, University of North Carolina, Chapel Hill, NC 27599, USA

wave (ILW) (Davis and Acrivos 1967; Kubota et al. 1978) and the Benjamin–Ono (B–O) equations (Benjamin 1986; Kalisch and Bona 2000). More recently, Choi and Camassa (1999) derived a fully-nonlinear model for internal waves in two-layer deep water configuration that makes no assumptions on the amplitude of the wave. The system of equations in the depth and the depth-averaged fluid velocity of the thin layer reduces the ILW and BO models in the appropriate weakly nonlinear, unidirectional limit, but can accommodate waves in the nonlinear regime as well. Mathematically, the intermediate long wave equation and its infinite-depth limit, the Benjamin–Ono equation, are completely integrable models for internal waves in deep water, and in principle allow for exact solutions to be computed. While these are certainly a desirable property of a physical model, the weak nonlinearity assumption excludes internal wave phenomena commonly seen in nature. In particular, wave amplitudes are observed to be of magnitudes several times the thickness of the upper layer of water, which falls well outside the weak nonlinearity assumption. The next step towards an accurate comparison can consist of modeling ISWs by solving the Dubreil–Jacotin–Long (DJL) equation (Dubreil-Jacotin 1934; Long 1953), which gives steady-state solutions to the Euler equations in the moving frame of the wave. While this approach does not have the appeal of analytical-type methods previously cited, it is not restricted to simple stratifications and provides an intermediate theoretical tool between direct, time-dependent numerical simulations and integrable or analytically tractable models.

Experimental and field observations are routinely compared with numerical solutions to support results extracted from field experiments and extrapolate integral quantities such as wavelength and wave speed (Vlasenko et al. 2000; Preusse et al. 2012a, b; Lien et al. 2012, 2014). Recently, Passaggia et al. (2018) used a DJL solution to compute waves corresponding to the field measurements of Moum et al. (2003) and provided an accurate representation of both waves and instability dynamics. Among the open problems in modelling the generation of ISWs, yet to be studied in detail, is the role of turbulent wakes that emerge during the generation phase while they are not fully separated by the laminar primary wave motion. In what follows, we indirectly address this issue by a systematic comparison of experimental data with analysis of the DJL equations and direct numerical simulations, with solutions and observations of waves both close to and far from their generation site.

Experiments in the miscible and shallow regime have been extensively carried out (see, e.g., Grue et al. 1997, 1999; Carr et al. 2008; Fructus et al. 2009; Carr et al. 2011, 2017). However, for the deep water regime, results of interfacial waves from experiments mostly used immiscible fluids (e.g. using water/petrol or water/silicon oil) see, e.g., Michallet and Barthélemy (1998) and Kodaira et al. (2016). To the best of our knowledge, the results presented herein are the first to be performed with miscible fluids on much larger scales than other experiments, both for the horizontal and/or the vertical length scales. The use of salt as a stratifying agent, plus the size of the domain, positively indicates that the results are representative across several length scales and indicate scalability to the extreme case of oceanic ISWs. This assertion is confirmed in the conclusions of the present study, where our experimental, numerical and theoretical results are compared with observations from field measurements taken near the Luzon strait for large amplitude internal solitary waves (Ramp et al. 2004; Huang et al. 2016).

In order to compare wave properties, we collect local profiles of fluid velocities and density from particle image velocimetry (PIV) and laser-induced fluorescence (LIF); these tools allow computation of amplitude, speed, and wavelengths from a dataset. These properties are then compared with DJL solutions and direct numerical simulations of the Euler equations. We show that experiments and simulations do capture the dynamics of internal solitary waves, and, in particular, we show that experiments closely reproduce the DJL predictions, thus also assessing the effect of a diffused interface. Direct numerical simulations of two-dimensional time evolution governed by the Euler equations are in good agreement with wave quantities. In contrast with DJL solutions, the time-dependent wave profiles clearly highlight a lack of fore-aft symmetry, which could be caused by dynamical interaction of the emerging (main) solitary wave with the wake from the generation site for traveling distances commensurate to those of the experiments.

Specifically, the paper is organized as follows: Sect. 2 presents a description of the experimental facility and details about the methods used to perform wave measurements. The numerical strategies are reported in Sect. 3 together with a description of the initial conditions used to replicate the dam-break problem. The results are summarized in Sect. 4 and discussed in Sect. 5 with respect to theoretical model predictions and discussed in perspective to field–field measurements.

2 Experimental setup

Experiments were conducted at the Joint Applied Mathematics and Marine Science Laboratory in Chapel Hill, North Carolina. Our approach is to generate internal solitary waves under stable continuous stratification in the modular wave tank of the Joint Fluids lab. The dimensions of our tank, 27 m long, up to 3 m high and 0.75 m wide (see Fig. 1a, b) allow us to reach larger scales than previously achieved in laboratory experiments, such as those reported in Koop and Butler (1981), Grue et al. (1999), Michallet and Barthélemy (1998), Kodaira et al. (2016) and Carr et al. (2017).

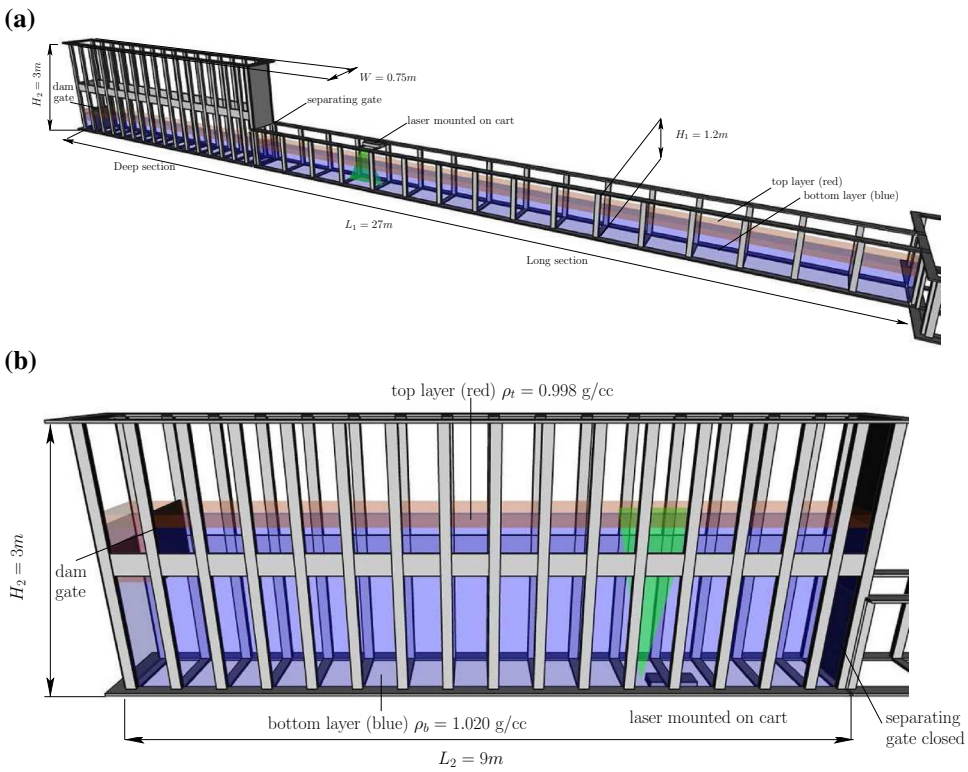

Fig. 1 Schematic showing the two sections of the modular wave tank for the long setup (**a**) and the deep setup (**b**)

The modular tank was setup in two different ways: a long and shallow experiment where the wave was propagated down the full length of 27 m, and a deep but shorter experiment where the wave propagated over 9 m in the 2.25 m deep section. In the deep setup, the base layer was 2.15 m deep whereas the top layer was 10 cm. In the case of long and shallow runs, the adjustable gate between the long and the deep sections remained fully open, for a total fluid depth of 77 cm consisting of a top and bottom layer of 15 cm and 62 cm, respectively (see Fig. 1a). This particular choice was made to match the experiments of Grue et al. (1999) in order to provide a term of comparison for our experimental data with the shallow configuration. The laser and the imaging system, consisting of a double set of a PIV camera and LIF cameras, all equipped with narrow band-pass optical filters—respectively, at 532 nm for the PIV and 583 nm for the LIF—were mounted on a computer-controlled motorized cart. The full setup was either kept in a fixed position or towed along the tank to track the spatio-temporal evolution of the waves as they traveled down the long section (see Fig. 1b). In the case of the deep, short runs, the adjustable gate was closed to create a water-tight seal between the deep and the long section. It will be shown later that these conditions are sufficient to generate nonlinear internal waves in the deep regime in a salt-stratified environment. The laser was mounted under the tank, and a single PIV/LIF setup was mounted on a fixed platform at the level of the top layer. In both cases, an 80 cm tall gate formed an "internal" dam that was either pulled up during the long runs or down during the deep runs in order to release the trapped fresh water.

Stratifications were generated by combining salt and fresh water to a desired salinity, and then pumping it into the flume from the adjacent storage and processing unit. This allowed for profiles within the tank ranging from a nearly two-layer structure to continuous stratifications of general form. All tank sides, including the bottom, consist of tempered glass panels, which allow for visualization from all directions. The flow was illuminated using a Litron® Nd:Yag diode pumped double cavity laser with 100 mJ per pulse at 532 nm wavelength used for both PIV and LIF (cf. Fig. 1a, b). PIV combined with LIF data were collected with a custom built camera setup using up to four GigE Bobcat B3320 Imperx® 8Mpx CCD cameras triggered simultaneously with the laser using a Stanford Research® DG535 pulse generator and acquired simultaneously on a computer using three Ethernet cards. The analysis of the experimental data was performed using the Matlab®-based open-source PIV software DPIVSoft (Meunier and Leweke 2003; Passaggia et al. 2012) to process the PIV and the LIF images. The resolution of the PIV/LIF was 0.0210/0.0212 cm/px in the deep case and 0.0302/0.0301 cm/px for the long setup. In addition to the stationary camera set-up, a moving camera mount followed and moved slightly faster than the wave in order to capture their evolutions over a longer distance.

Initial density measurements were acquired at 0.5 cm interval in depth, using an Orion TetraCon® 325 conduc-

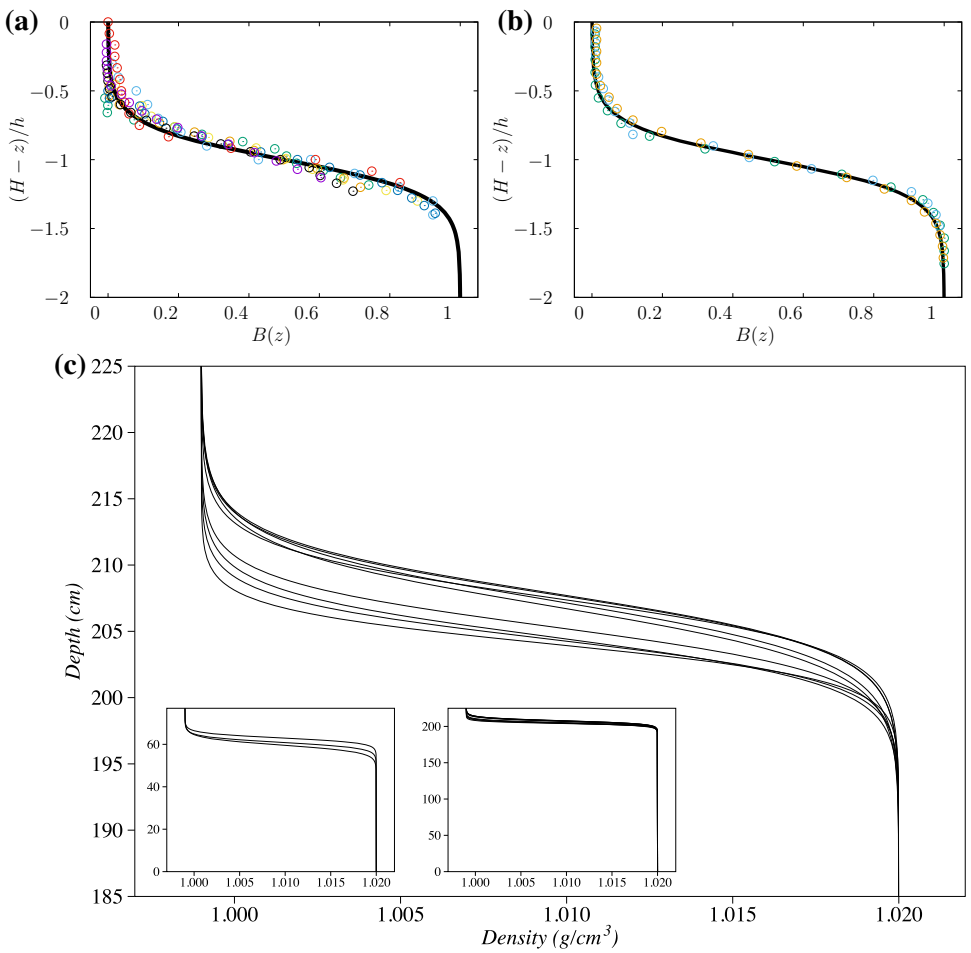

Fig. 2 Background density profiles extracted from the experiments and used in both numerical simulations and DJL calculations. **a** Initial profiles normalized with respect to the reference profile $B(z) = (\tanh(4(z+1)) - 1)/2$ in the deep/short configuration and **b** in the long/shallow configuration. **c** Details of the background stratification showing the variability of the height and thickness of the pycnocline between experiments for the deep regime. Insets: comparison between long/shallow configuration (left) and deep/short configuration (right)

tivity probe connected to a WTW Cond® 197I conductivity meter, which was then checked against the known bottom-layer salinity in parts-per-thousand, verified using a Anton® Paar DM35 densitometer whose calibration was verified to the fourth digit. Initial density profiles were measured before each experiment using the Orion TetraCon® 325 conductivity probe mounted on a Velmex® linear stage. Measurements of conductivity and temperature were collected every centimeter and interpolated to calculate the corresponding density profile. These initial vertical profiles of density are shown in Fig. 2a–c for both the deep and the long section. In particular, with $\rho(z)$ the density at the vertical location z, and $\Delta\rho$ the total density variation from bottom to top (with reference density ρ_0 being the minimum density), we denote hereafter the renormalized density profile by $B(z)$, where

$$B(z) = \frac{\rho(z) - \rho_0}{\Delta\rho}; \tag{1}$$

this is shown in Fig. 2a in the case of the deep configuration and Fig. 2b for the long/shallow configuration.

The top layer was dyed with 0.066 µL per liter of water using BrightDyes® Rhodamine WT. Lavision® nearly neutrally buoyant polydisperse polyethylene PIV particles with diameters in the range [10:100] µm were wetted beforehand with the top layer fluid, mixed in a separate tank, sprayed over the free surface, and left to slowly settle across the layers to seed the experiment. Note that the settling speed was several orders of magnitude smaller than the speed of the waves. The laser was double-pulsed at 3 Hz while image pairs were recorded by mean of double exposure with a 20 ms difference between two successive frames. The camera set-up was centered at 2.46 m from the end of the tank, or 15 m from the end of the long experiments. The purpose of this location was to capture a well-developed (i.e. sufficiently separated from the wake) solitary wave while minimizing end effects.

In our experimental facility, the salt water is recycled after each experiment. It is sent to a reverse osmosis unit which separates the salt component and is subsequently filtered using a carbon and UV filters. The recycled water out of the reverse osmosis unit is then sent to 15 storage tanks containing up to 23 m^3 of brine (six tanks) and fresh water (nine tanks).

3 Numerical methods

We consider the dynamics of an inviscid incompressible fluid governed by the Euler equations, restricted to two-dimensions,

$$u_t + uu_x + wu_z = -\frac{p_x}{\rho}, \tag{2a}$$

$$w_t + uw_x + ww_z = -\frac{p_z}{\rho} - g, \tag{2b}$$

$$\rho_t + u\rho_x + w\rho_z = 0, \tag{2c}$$

$$u_x + w_z = 0. \tag{2d}$$

Viscosity is neglected throughout this study, as the Reynolds number, based on either fluid or wave speed is sufficiently large. For typical experiments in our facility, these are, respectively, $Re_{\mathrm{F}} \simeq 6 \times 10^4$ and $Re_{\mathrm{W}} \simeq 1.4 \times 10^5$). In the notation above, (u, w) are the horizontal and vertical fluid velocities, respectively, ρ is the (variable) fluid density, and p is the pressure. Throughout the present manuscript, subscripts indicate partial derivatives. These equations are discretized and solved using the VarDen algorithm (Almgren et al. 1998) with initial conditions chosen to match those in the experiments. The numerical strategy of the VarDen code uses a second-order accurate projection method and a second-order predictor-corrector scheme for time integration. Both time-step and spatial mesh are adaptive with a base mesh discretization of $\Delta x \approx 0.44$ cm and $\Delta x \approx 0.30$ cm in the deep and long cases, respectively. VarDen employs adaptive mesh refinement by doubling the spatial refinement according to the criteria developed in (Bell et al. 1994), which tests convergence by comparing the coarsest grid and a once-refined grid. The time-step is adjusted automatically to maintain the CFL number. The grid refinement is performed up to six levels, giving a maximum resolution of $\Delta x \approx 6.9 \times 10^{-3}, 4.7 \times 10^{-3}$cm in the deep and long cases, respectively. With the maximum resolution, the pycnocline can contain up to a thousand grid points.

The initial conditions for the dam-break are approximated using a hyperbolic tangent function profile given by

$$\rho(x, z) = \overline{\rho}\left(z - \frac{H_{\mathrm{gate}}}{2}\left(1 + \tanh(W_{\mathrm{gate}} - x)\right)\right), \tag{3}$$

where $\overline{\rho}(z)$ is the background density, W_{gate} the width of the gate (fixed at 56 cm in both experiments and simulations) and H_{gate} is the depth of the fluid behind the gate beyond the rest state. The background density $\overline{\rho}$ is assumed to be a hyperbolic tangent function and it is best-fit to match the density profile measured before each experiment. Boundary conditions are taken to be free-slip, no-flux walls including the top of the domain; this rigid lid assumption could be viewed as the most significant departure of the simulations from the experiments. However, this is expected to cause negligible effects given the bounds on density differences, although our results do show a legacy of weak free-surface effects (cf. Sect. 4). One phenomena of interest that was not addressed is the interaction between the bottom boundary layer and the ISW (Carr and Davies 2010; Sadek et al. 2015), but this deserves a study that is left for a future investigation.

The dam-break method of generation and finite domain of the tank preclude true traveling waves from being observed experimentally. For point of comparison, however, we include the predictions of the DJL equation

$$\nabla^2\eta + \frac{N^2(z-\eta)}{c^2}\eta = 0, \tag{4}$$

in which η is the vertical displacement of a given isopycnal (constant ρ) line, $N^2(z-\eta) = -g\overline{\rho}'(z-\eta)/\overline{\rho}(z-\eta)$ is the Brunt–Väisälä frequency, and c the speed of the traveling wave. The DJL equation is a reduction of the Euler equations to a steady waveframe $x \to x - ct$, and here we used the Boussinesq approximation version, whereby density variations are neglected for the inertial forces. The DJL equation has a natural variational formulation, so by using an iterative method that minimizes the energy traveling wave solutions can be computed efficiently (Stastna and Lamb 2002). The present results are evaluated using the multi-grid strategy of Dunphy et al. (2011), with the DJL solutions obtained by continuation with increasing energy using fixed point iterations. The domain sizes for the DJL solver were $[L, H] = [9, 2.15]$ m for the deep case and $[L, H] = [9, 0.77]$ m for the long tank. The discretization consisted of equi-distributed points on a multi-grid strategy starting from $[n_x, n_z] = [256, 256]$ for the coarse grid and up to $[n_x, n_z] = [2048, 2048]$ in the case of the fine grid for the DJL solver. Convergence was also made possible starting with a thicker interface and was progressively decreased through four levels of refinement down to the target thickness value.

The stratification at $x \to \pm L/2$ was kept constant and set by a hyperbolic type tangent of the form

$$\overline{\rho}(z) = \rho_0 + \frac{\Delta\rho}{2}\left(1 + \tanh\left(\frac{z - z_0}{\delta}\right)\right), \tag{5}$$

where $\rho_0 = 0.998$ g/cc is the reference density of the fresh water, measured at room temperature at $T = 23\,^{\circ}$C, $\Delta\rho$ is the maximum density difference measured between the top and the bottom of the tank, δ is the parameter that defines the thickness of the pycnocline, and z_0 is the height of the inflection point of the density profile. The initial condition together with wave profiles is provided in Fig. 3a at $d/h = 5$ for the deep configuration and in Fig. 3b at $d/h = 2$ for the long configuration. The different profiles show the horizon-

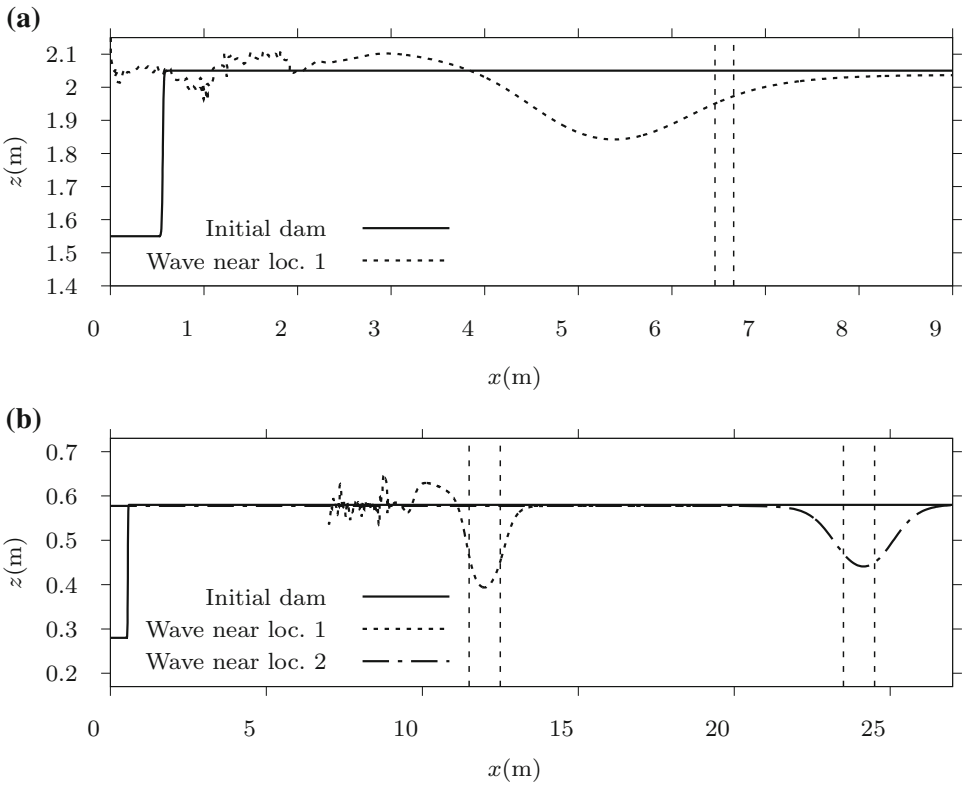

Fig. 3 Initial condition and snapshot of wave evolution at later times for **a** the deep configuration, **b** the long configuration captured by the simulation. The wave profiles are isopycnal position of $z(B = 0.5)$ for the three locations where measurements were taken. The vertical lines mark these locations in the plot

tal isopycnal position of $z(B = 0.5)$ for different locations where measurements have been performed.

4 Results

Direct numerical simulations of the initial value problem for the dam-break-type initial solution are compared with experimental results and traveling-wave solutions computed from the DJL equations. In what follows, we first report a comparison for wave properties between the three methods and show that onset of nonlinear internal solitary wave propagation is observed in deep water from fixed location measurements. Next, horizontal wave profiles from fixed measurements are analyzed for both deep and long configurations. Finally, in Sect. 4.4, similar properties are examined but for data collected from a moving frame, whereby internal solitary waves are being tracked along the long section, in both the experiment and the simulation, to investigate their spatio-temporal evolution.

4.1 Measurements from stationary locations

The results were extracted from the LIF and PIV data as illustrated in Fig. 4a–c for the deep setup and Fig. 4d–f for the long setup. The spatio-temporal evolution of the waves in both the deep and long experiments are shown by means of density identified from the LIF, used as proxy and velocity computed using PIV. Figure 4d–f shows the largest amplitude wave generated in the long tank and replicates the waves measured by Grue et al. (1999). The particular wave shown in Fig. 4a is compared with a much larger wave obtained in the deep tank in Fig. 4c. The experiments in the long configuration were repeated multiple times to check for the consistency of the generation mechanism, using similar initial density profiles as shown in Fig. 2, and the results are displayed for both experimental data, DJL predictions and DNS simulations in Fig. 6a–d. Instantaneous profiles of horizontal velocity and density (through the proxy by LIF) are shown in Fig. 5a at $x/h = 70$ from the dam gate for the deep case and Fig. 5b at $x/h = 80$ for the long case. These measurements are compared with the companion DNS of the initial value problem and the DJL results. The error measured between the simulation and the corresponding experiments at the location of maximum wave amplitude $\eta_{\max}$ is less than 10% between the simulation and the DJL profile and 4% between the experiment and the direct numerical simulation. Both the amplitude and the velocity are closely predicted for the deep and the long experiments. Here, the DJL solutions were computed by matching the amplitude with the experiment. The overall agreement is satisfactory, and the results, including measurements from other waves, show a slight improvement of the comparison with increasing amplitude. Note that near the surface the density profile inferred

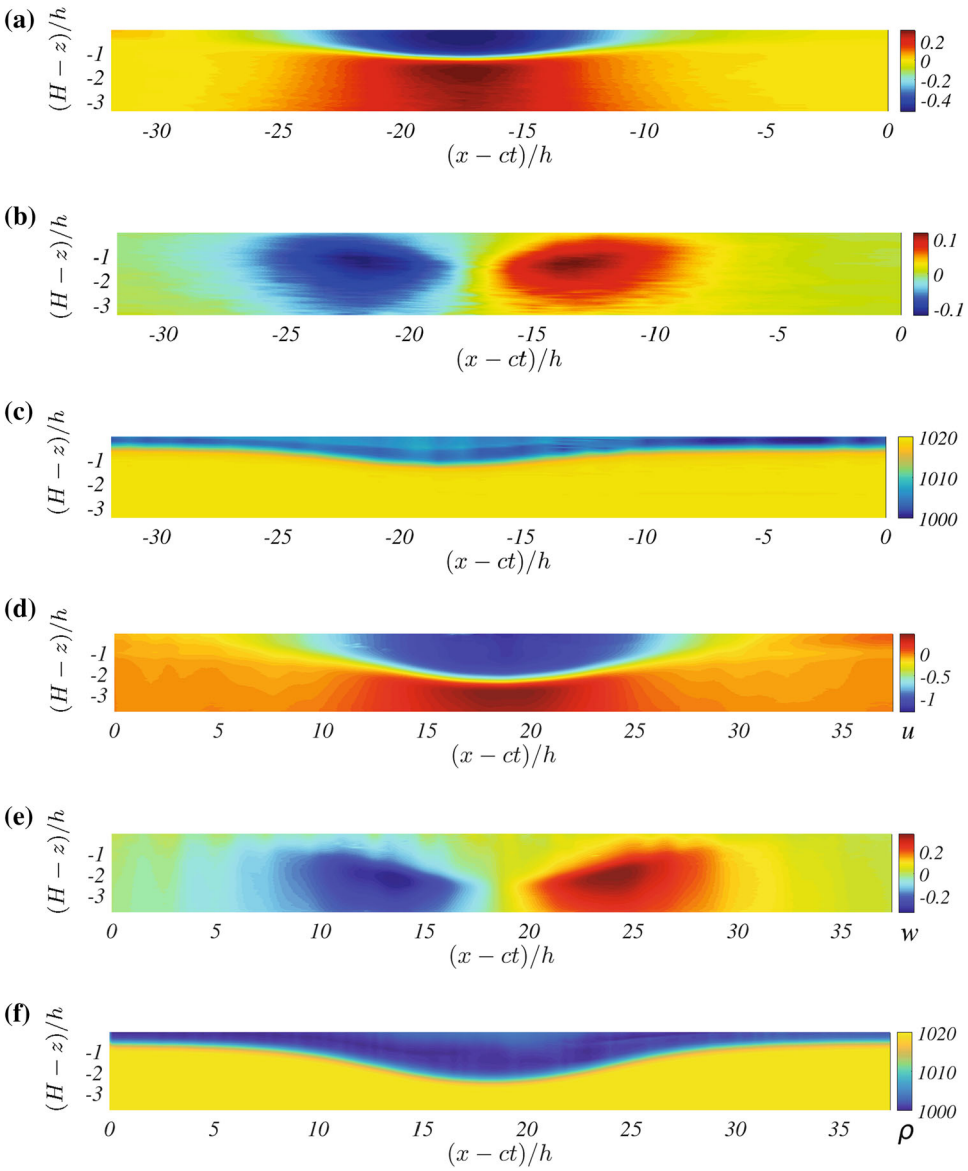

Fig. 4 Example of internal wave data in experiments for the long/shallow setup: **a–c** horizontal velocity field $u((x-ct)/h$ vs. $(H-z)/h)$, vertical velocity $w((x-ct)/h$ vs. $(H-z)/h)$ and density field $\rho((x-ct)/h$ vs. $(H-z)/h)$, respectively, for a dam height $d/h = 6 \pm 10\%$, and a thin pycnocline $\delta/h \approx 0.55$, corresponding to $c/\sqrt{g'h} \approx 1.43$, $a/h \approx 0.718$ and $\lambda/h \approx 5.04$. **d–f** Similar to **a–c** but for a dam height $d/h \approx 2 \pm 10\%$, and a thin pycnocline $\delta/h \approx 0.4$, corresponding to a wave with characteristics $c/\sqrt{g'h} \approx 1.748$, $a/h \approx 1.544$ and $\lambda/h \approx 3.329$

from LIF data departs from the simulation, due to either light absorption by the dye (cf. Fig. 5a) or uneven concentration due to fading at this particular location in the tank (cf. Fig. 5b). The size of the facility, and the length of time for the set up of each experiment, made the dye intensity difficult to control. It is also interesting to notice that the vertical wave profile for the larger amplitude waves exhibits vertical oscillations, shown in Fig. 4b, which appear to be synchronized with the oscillations of the free surface (not shown here). The wavelength of this oscillation is much shorter than the wavelength of the internal solitary wave and seems to be dominant near the front of the wave, a feature that agrees with the ones recently reported by Kodaira et al. (2016) for large-amplitude interfacial ISWs in immiscible fluids.

4.2 Global ISWs characteristics

Wave characteristics defined by amplitude a, wave speed c and effective wavelength λ/h are shown in Fig. 2a–d, where the full symbols represent the results extracted from the two-dimensional Euler simulations, and the hollow symbols with error bars depict the experimental results. All results are non-dimensionalized by the characteristic depth h given by the mean-density isoline in the rest state, and the characteristic velocity $c_0^2 = g\,(\rho_{\max}/\rho_{\min} - 1)\,h$. The wave speed c was measured using two temporal mean-density displacement profiles located at fixed locations in the tank and separated by a distance $\Delta x \approx 25$ cm apart from each other. Similarly to the experimental investigations of Luzzatto-Fegiz and Helfrich (2014), the velocity was computed by minimizing the time difference τ between the two temporal profiles, with the wave

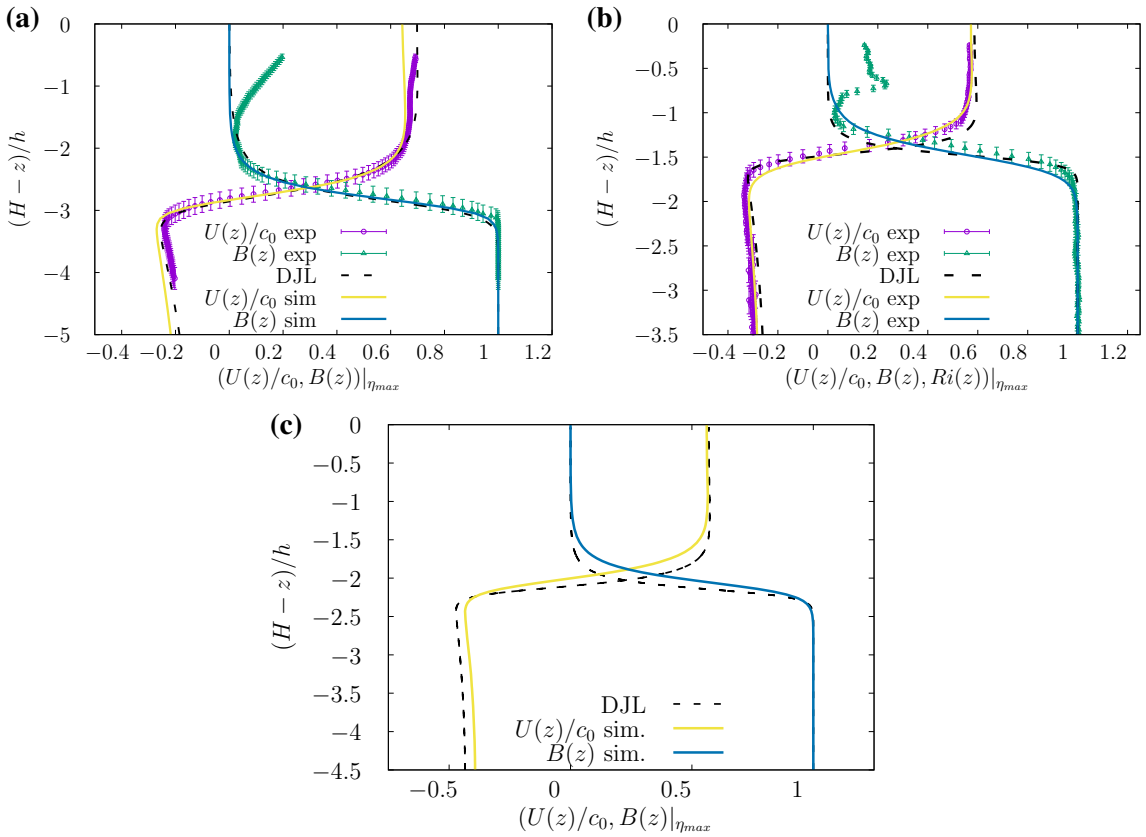

Fig. 5 Example of velocity profiles $u(z)$ and density profiles $b(z)$ extracted from the PIV and LIF data at the center (maximum pycnocline displacement) of a wave, collected along the wavetank at different distances x from the generation gate; **b** long/shallow configuration, $x/h = 85$; **c** long/shallow configuration, $x/h = 65$

velocity calculated using $c \approx \Delta x/\tau$. Once determined, the speed of the wave was used to transform the temporal scale t to the spatial scale X through the transformation $X = x - ct$. The effective wavelength λ/h is defined as

$$\lambda = \frac{1}{a}\int_0^\infty \zeta(X)\mathrm{d}X \tag{6}$$

with $\zeta(X) = \zeta(x - ct)$ the displacement of the mean-density isoline, but computed in practice by integrating in time along the transformed spatial axis X from the beginning of the experiment until the crest of the wave is observed in both the experiments and the numerical simulations.

The amplitude, both experimentally and numerically, of each ISW as a function of the dam height is shown in Fig. 6a, where the response of the ISW amplitude a/h to increasing dam height d/h remains essentially linear. This relationship indicates the consistency of the generation mechanism and the clear relation between dam height and resulting solitary wave amplitude. This confirms that the present experiments essentially lie within the deep regime, because no saturation of amplitude with dam height was observed, as it would be expected for the shallow regime when approaching a conjugate state. The normalized effective wavelength λ/h as a function of the wave speed is shown in Fig. 6b, which shows that our measurements are well within the transition from linear to nonlinear internal solitary waves. The DJL solutions, depicted by means of solid and dashed black lines for the thicker and thinner pycnoclines in Fig. 6b–d, both describe a minimum effective wavelength λ/h as a function of the wave speed $c/\sqrt{g'h}$. The critical point found in the vicinity $[\lambda/h, c/\sqrt{g'h}] \approx [4, 2]$ by the DJL computation is confirmed by the numerical simulations with a thin pycnocline [shown by means of red triangles (▲)]. This critical point is also captured by the experiments and associated DNS, although the thicker pycnoclines suggest that this minimum shifts to slightly lower values of both λ/h and $c/\sqrt{g'h}$.

The normalized speed $c/\sqrt{g'h}$ is displayed as a function of the amplitude a/h in Fig. 6b, where the DJL prediction is found to closely predict the speed simulated by the nearly two-layer stratification shown by the red triangles. The ISWs' speed are well within the bounds predicted by the DJL calculations except for the three larger amplitude experimental

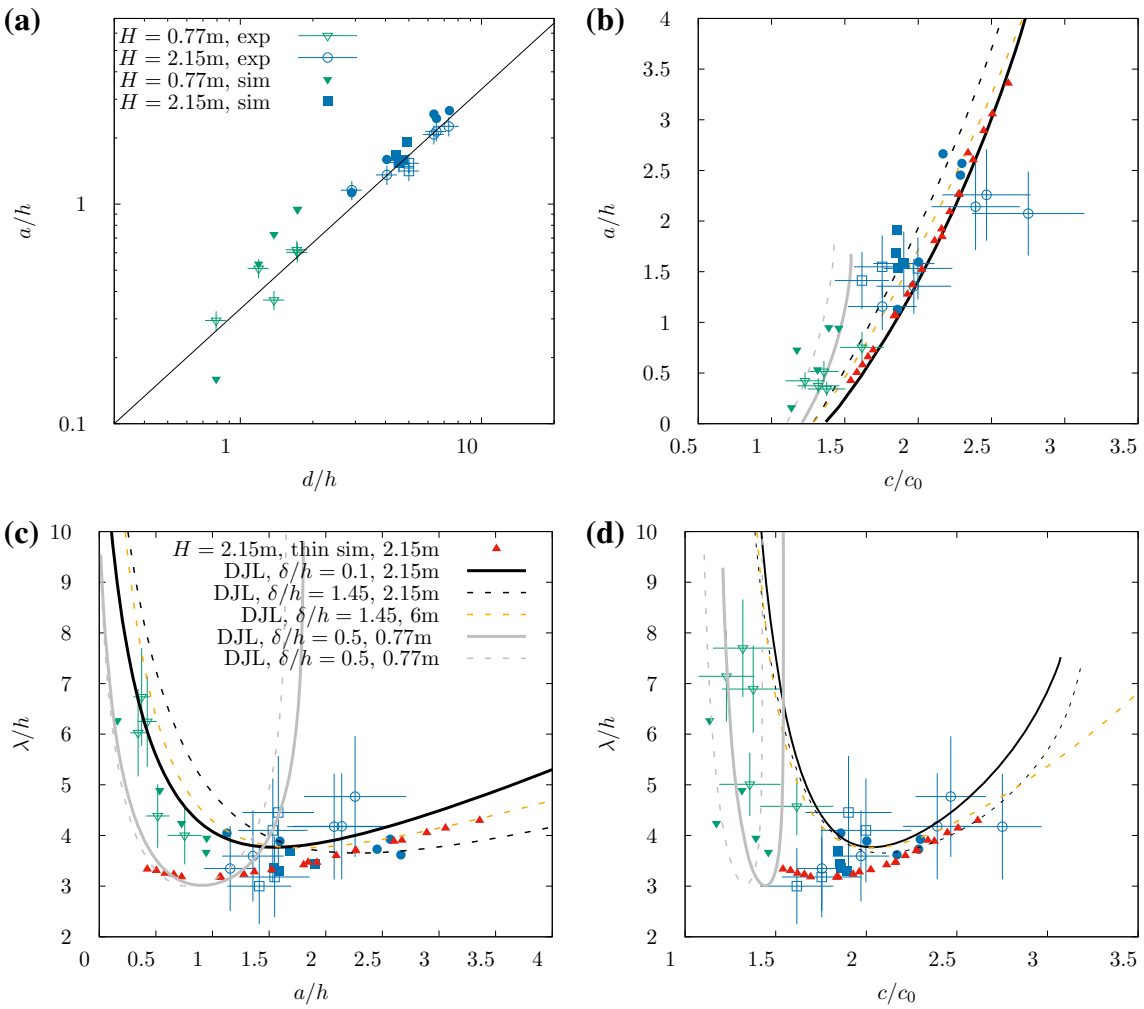

Fig. 6 ISW characteristics, summary of all simulations and experiments: **a** ISW's amplitude a/h as a function of the dam height d/h, **b** amplitude a/h as function of wave speed $c/\sqrt{g'h}$, **c** reduced wavelength λ/h as function of wave amplitude a/h, and **d** reduced wavelength λ/h as function of wave speed $c/\sqrt{g'h}$. The full symbols show the numerical simulations, the hollow symbols with error bars refer to the experiments, and the solid and dashed curves are the theoretical predictions from the DJL equation at various locations and diffused interface thicknesses, as labeled in the legends

waves, which appeared to be faster than both the DJL prediction and the respective numerical simulations. However, a closer look at the PIV and LIF data shows that these waves were strongly asymmetric, with what appeared to be a recirculating core, from which large-amplitude billows were observed developing downstream. Note that, for these particular waves, the stratification was the most diffused, which favors the development of recirculating cores, also known as solicores (Luzzatto-Fegiz and Helfrich 2014).

Figure 6c depicts the effective wavelength λ/h as a function of the ISWs' amplitude a/h, where a good collapse between theory, numerical simulations, and experiments is further confirmed. The DJL results show the effect of pycnocline thickness, parametrized in nondimensional form by δ/h, on the wave properties. As δ/h increases, the critical amplitude a/h at which the minimum of the effective wavelength $\lambda(\delta/h)$ occurs also increases, while λ/h appears to remain essentially independent on the thickness in the range of pycnoclines measured in our experiments, from $\delta/h = 0.1$ for the thinnest to the thicker values of $\delta/h = 1.45$.

Similar conclusions can be drawn from Fig. 6d where the effective wavelength λ/h is reported as a function of the non-dimensional wave speed c/c_0. The collapse between simulations and experiments is well within the DJL predictions where the thickness of the pycnocline does not seem to play an important role.

4.3 Wave profiles

The errors in the collapse between the DJL wave properties, the experiments, and the numerical simulations suggest that the wave profiles provide more insights into wave details such

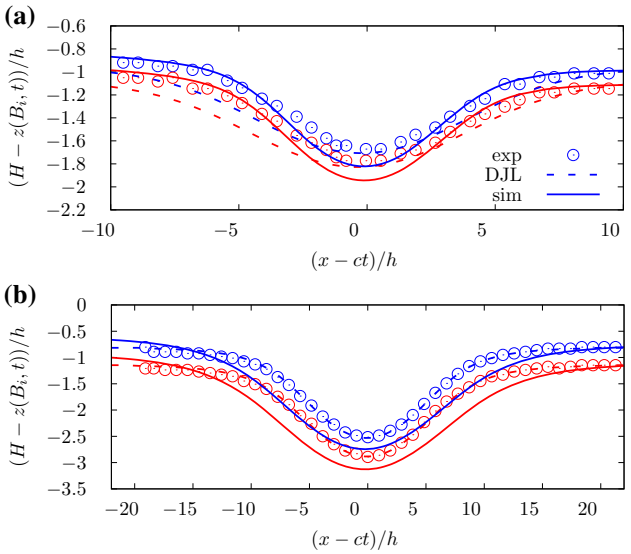

Fig. 7 Height of constant density $z(B_i, t)$, where B_i is a given value with $i = [1, 2]$, in for a long experiment (**a**) and a deep experiment (**b**) in the time–space coordinate $(x - ct)/h$. The dashed lines are iso-density of the thirtieth (blue) and seventieth (red) percentile of the density, corresponding to $B_1 = 0.3$ and $B_2 = 0.7$, respectively

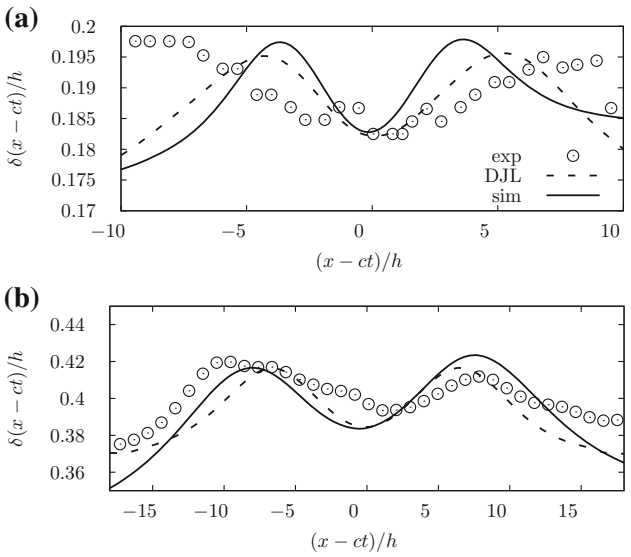

Fig. 8 Thickness $\delta(x - ct)$ of the diffused interface, measured by the difference between the thirtieth and seventieth percentile of the density reported in Fig. 7a, b for: **a** the long configuration, and **b** the deep case in the time-space coordinate

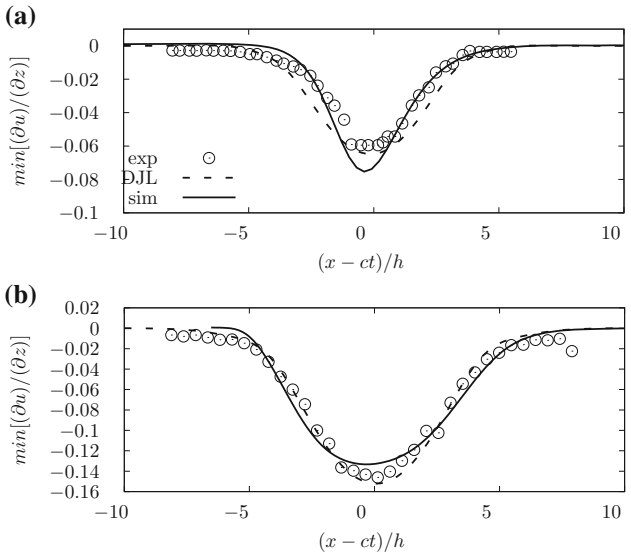

Fig. 9 Minimum value of the shear $\partial u(x - ct, z)/\partial z$ computed along the waves reported in Fig. 7a, b for the long (**a**) and deep (**b**) cases in the time–space coordinate

as symmetry and the effects of wakes. The DJL solutions of the Euler equations are symmetric, traveling, steady-states waves in the moving frame of reference $X \rightarrow x - ct$. In contrast, we are interested in comparing wave profiles for both experiments and numerical simulations, which are developing solitary waves that have not yet reached an asymptotic steady state (which of course could only be achieved adiabatically with respect to the slow decay due to the presence of viscosity in real experiments). Profiles of solitary waves are shown in Fig. 7a for the long configuration and Fig. 7b for the deep experiments tracking isopycnals from the experimental data, by matching the dye intensity with the corresponding value of the density. Values of the thirtieth and seventieth percentile of the density are reported in Fig. 7a, b, where the amplitude of the DJL solution was matched with the experimental results. The collapse between experiments and the DJL profile is particularly striking for the deep case. While the numerical simulation are in good agreement with DJL profiles, apart from a slight asymmetry with respect to the trough of the wave in Fig. 7b, the experimental and numerical results seem to degrade with respect to the DJL solution for the smaller amplitude wave shown in Fig. 7a. Despite the small mismatch in amplitude, the asymmetry between the leading and the trailing edge of the wave seems to be more important than for its large-amplitude counterpart. The most likely scenario for this discrepancy seems to be related to the lack of separation from the wave's wake, wherein large amplitude, two-dimensional structures are seen to persist in the numerical simulations. This asymmetry is a consequence of the generation mechanism, which we show in the next section to be less apparent as the ISW travels farther along the wave tank. Of course, to increase the fidelity of the simulations with respect to experiments the former would have to be implemented in fully three-dimensional settings, substantially increasing the computation cost.

The difference between the two isopycnals difference $\Delta\delta/h$ above is shown in Fig. 8a, b for both the deep and the long case, respectively, where we aim at confirming that

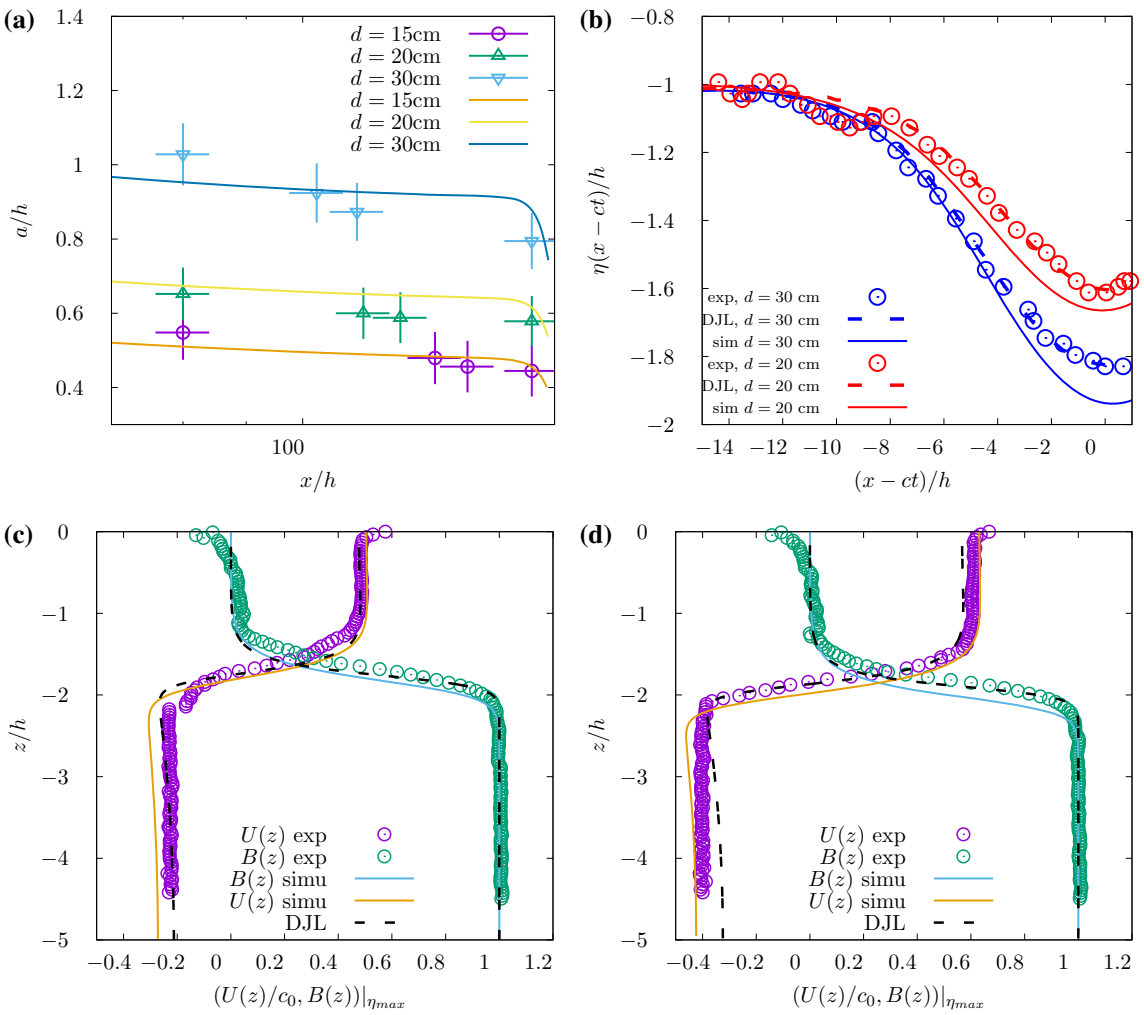

Fig. 10 Wave properties from moving frame: **a** normalized ISW amplitude a/h as a function of the non-dimensional cart position x/h tracked in the long section for three representative dam height. **b** Profiles of the fiftieth percentile of the density inferred from the LIF measured at $x/h \approx 160$ from the dam for an initial dam heights. $(d-h)/h \approx 1$ (red) and $(d-h)/h \approx 2$ (blue). Profiles of horizontal velocity (purple–orange) measured by PIV (symbols) and normalized density $B = (\rho(z) - \rho_{\min})/(\rho_{\max} - \rho_{\min})$ (blue–green) inferred from the LIF at the position of maximum displacement $\eta_{\max}$ compared with the DJL solution (lines) computed for the same amplitudes at $(d-h)/h \approx 1.33$ (**c**) and $(d-h)/h \approx 2$ (**d**)

the expansion and compression of the isopycnals induced by the wave can be observed in the experiment and is captured by the DJL and direct numerical simulations (and has been modeled in Camassa and Tiron 2011). In the long/shallow case, Fig. 8a shows this comparison between the DJL solution, the simulation, and the experiment. At the leading side of the wave, the isopycnals undergo an expansion, followed by a compression at the trough and a re-expansion along the lee side. The comparison between the DJL waves and the simulations is in good qualitative agreement for both amplitude and locations of compression and expansion. The comparison with the experimental data is less precise, and it is barely captured for the experiments in the long configuration (see Fig. 8a) where the variations are only of the order of $\approx 1.5\%$ of h. The comparison and agreement in the deep case and a larger amplitude wave is more striking (see Fig. 8b). Variations in the pycnocline thickness are found to be of the order of $\approx 5\%$ of h for the numerical simulation as well as for the DJL wave and the experiment.

Finally, we report the minimum value of the shear computed from the DJL solution, the experiment, and the numerical simulation in Fig. 9a, b for the short/deep and the long/shallow cases. The collapse between experiments, DJL solutions, and numerical simulations is well predicted for both cases. This plot tests the quality of our experimental and numerical approaches. In the next section we extend the present analysis beyond the scales previously reported by Grue et al. (1999) for the long/shallow regimes and investigate the evolution of these ISWs by tracking their spatio-temporal evolution. To the best of our knowledge, this

is the first time that such measurements with data collected in the co-moving frame of the wave have been attempted. This helps determine the trend of our waves in eventually reaching a traveling (adiabatic) steady state form farther down the long section.

4.4 Measurements from tracked ISWs

The discrepancy for the measurements performed at 12 m from the gate in the long section led us to track several ISWs by following them with the moving motorized cart shown on top of the long section in Fig. 1. Once the ISWs were seen to pass the first location at $x = 12$ m, the cart was started with a velocity 10% greater than the traveling wave speed for a KdV solitary wave (Choi and Camassa 1999)

$$c = c_0 \left(1 - \frac{a}{2} \frac{\rho_1 (H-h)^2 - \rho_2 h^2}{\rho_1 h (H-h)^2 + \rho_2 h^2 (H-h)}\right).$$

Tracking ISWs remained, however, a difficult task due to the variability of wave speed immediately after the generation. We report only a limited number of measurements in Fig. 10a–d for 3 ISWs with initial dam heights $d = [15, 20, 30]$ cm. The maximum amplitude, measured using both the LIF and the region of maximum shear in the PIV is reported in Fig. 10a as a function of the distance traveled x/h. The amplitude of these waves was found to decay slowly as they travelled along the 27 m of the long section of our modular tank; this decay became less pronounced as the waves separated from their wakes. It is interesting to notice that both numerical simulations and experiments show a decay of the wave amplitude as the ISWs travel farther down the long section (Grimshaw et al. 2003). We remark that the simulation solves the Euler equation and does not include viscosity, the only source of dissipation being induced by the numerical scheme itself. Also, we remark that the larger amplitude ISWs measured in the experiment seem to decay faster than the amount predicted by the simulation. This could be attributed to the vibrations induced by the cart carrying the laser, cameras, and power supplies, which can inject noise in the fluid flow, as discussed below.

Measurements of wave profiles inferred from the LIF are shown in Fig. 10b for two representative amplitudes and compared with DJL solutions for the lee-side of the waves, where an overshoot was originally observed at $x/h = 80$. The collapse between experiments and theory appears to improve significantly, except for the near-wake region. Here transient growth of finite amplitude noise, induced by the vibrations of the cart, may be responsible for the transition to Kelvin–Helmholtz-type instabilities which are seen as oscillations at both the trough, the lee and more strikingly in the wake of the wave (Camassa and Viotti 2012; Passaggia et al. 2018). Note that stationary measurements, which did not induce

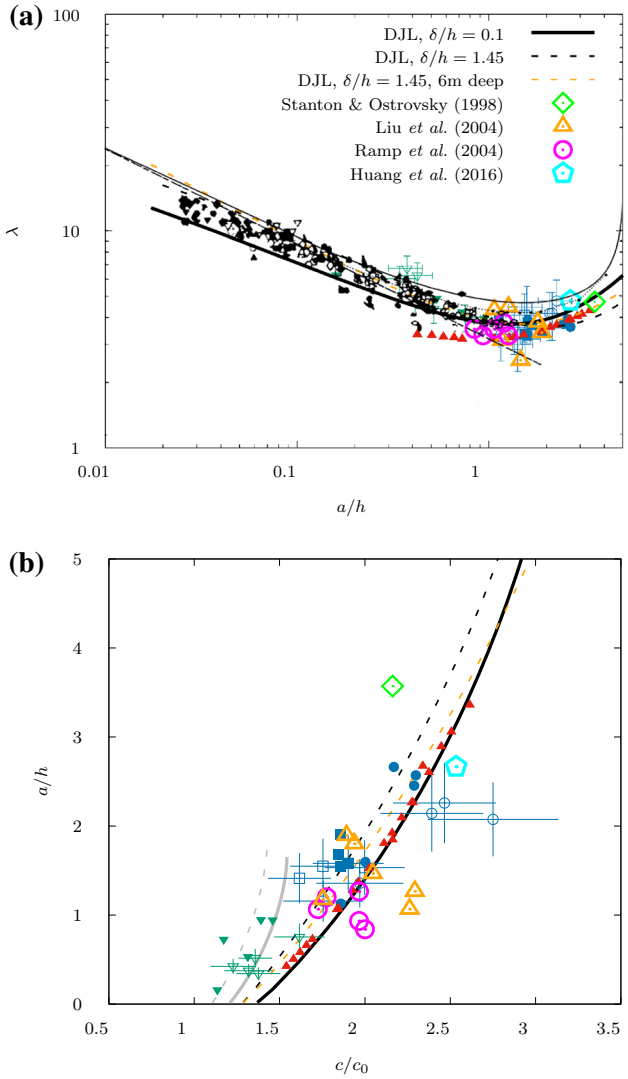

Fig. 11 Effective wave length λ/h as a function of wave amplitude a/h for the present results in salt - stratified water compared with previous experimental results from Koop and Butler (1981) (black symbols) for the case of immiscible fluids (water and freon), the KdV prediction (thin dashed line), two-layer model Grue et al. (1997) (thin dashed-dotted line), fully nonlinear model (line) Choi and Camassa (1999, 1996) in the long/shallow case, the field data of Liu et al. (2004) (large hollow triangles), Ramp et al. (2004) (large hollow circles) and Huang et al. (2016) (large hollow pentagon). Thick lines are the DJL predictions shown in Fig. 6c. **b** Same as Fig. 6c but compared with field data from the above references

such vibrations, displayed no noticeable growing transient inside the wave region.

The good agreement in Fig. 10b suggests that the ISWs are becoming close to a traveling wave-type solution. To support this conclusion, profiles of density measured at the trough of the ISWs, inferred from the LIF for the density and horizontal velocity measured from PIV, are compared in Fig. 10c, d for two representative waves. Both profiles appear to be in very good agreement between DJL and the simulations. Furthermore the overshoot observed at $x/h \approx 80$ has now

disappeared, and while horizontal velocity near the bottom shows a slight mismatch of the order of 8%—probably due to finite tank effects—the overall agreement is excellent. This suggests that our ISWs have to travel a distance of $x/h \approx 120$ from their generation site to more closely approach a traveling wave-type state.

The possible application of our results in the context of open ocean measurements and theoretical models is further discussed next, together with our conclusions on the present study.

5 Discussion

The present study reports a clear experimental evidence of nonlinear ISWs in the deep regime and miscible fluids. Results are systematically compared with DJL solutions, direct numerical simulations of the dam-break initial value problem, and the associated experiments. Measurements are reported for the fully nonlinear regime in a deep configuration, past the critical point, which is confirmed by the DJL theory where the nondimensional effective wavelength increases with respect to both the wave amplitude and wave speed. These results are supported with local measurements of LIF and PIV, which are further compared with the DJL waves and the direct numerical simulations with an overall satisfactory agreement. In addition, we explore the effect of the interface thickness on the dynamics and show that thick pycnoclines modify both wave amplitude and wave speed. Larger thicknesses increase the wave amplitude while decreasing the speed and the wavelength, an effect that does not seem to be experimentally studied in the same depth of other properties of internal waves.

Vertical and horizontal wave profiles are also compared between numerical simulations, experiments, and DJL solutions. For these properties, such velocity and density measurements, the agreement is excellent. Horizontal profiles of isopycnal displacement demonstrate the overall good agreement between the DJL solutions, numerical simulations, and experiments. We show in the long/shallow configuration that waves measured too close to their region of generation tend to be asymmetric, as they have not yet fully separated from their wakes. This effect is, however, not observed farther down the long section and shows that relatively large experimental facilities are necessary in order to observe the approach to true traveling waves in the mathematical sense of models such as KdV, DJL, and Camassa–Choi (Korteweg and De Vries 1895; Dubreil-Jacotin 1933; Choi and Camassa 1999; Camassa et al. 2006). Such asymmetries have also been reported in oceanic observations and are known to play an important role in the redistribution of nutrients and chlorophyll, which are essential drivers of primary production in the euphotic zone (Dong et al. 2015).

The present results are gathered in Fig. 11a together with the results from Koop and Butler (1981) where interfacial ISWs were generated in immiscible fluids (water and liquid freon) and the linear/nonlinear theories for the deep and shallow cases. In addition, we report large-amplitude ISWs wave characteristics from field measurements in the deep regime, in the case of a train of internal solitary waves propagating westward off the Oregon Shelf with very thin stratification (Stanton and Ostrovsky 1998) (◇). We also compare with ISWs propagating westward from Luzon straight in the South China Sea from Liu et al. (2004) (○) and Ramp et al. (2004) (△), and an extreme wave developing eastward in the Northern China Sea (Huang et al. 2016) (⬠). Effective wavelengths λ/h for both DJL, experimental, and field measurements are reported in Fig. 11a as a function of wave amplitude a/h. As displayed by this figure, our measurements fill the gap between the two-layer experiments of Koop and Butler (1981) and Michallet and Barthélemy (1998) and field measurements of large-amplitude ISWs in deep waters. At this point, a remark is in order: while experiments producing nonlinear ISWs could be performed in tabletop set-ups, our experiments further extend the range to larger scales (tens of meters) and move towards mimicking the dynamics of field observations (as mentioned above, typical Reynolds numbers are between 10^4 and 10^5). In turn, we observed large-scale effects such as transient growth and free-surface motions. The consistency of results across length-scales suggests that laboratory ISW characteristics faithfully represent ISWs measured from field observations. Wave speeds from field measurements are also compared with the DJL solutions, experimental data, and numerical results in Fig. 11b, which shows an overall good agreement. These data support the idea that large-amplitude ISWs in the nonlinear regime from field observations in the ocean (Stanton and Ostrovsky 1998; Huang et al. 2016) or in lakes (Preusse et al. 2012a, b) are only accurately modelled by DJL type solutions (Dunphy et al. 2011) and nonlinear theories such as the Choi–Camassa two-layer model (Choi and Camassa 1999).

PIV results and images from experiments indicate the presence of small surface waves traveling with the ISW for the larger amplitude ISWs. The resonance between capillary and gravity waves has been recently explored experimentally and theoretically for interfacial ISWs in immiscible fluids by Kodaira et al. (2016). Our numerical code is based on a rigid lid approximation, and thus cannot accommodate free surface motions. The present experimental results could, however, provide an interesting starting point to study surface-internal wave interactions in the case of miscible fluids, which deserves more investigation and represents an important application for the dynamics and prediction of large-amplitude internal solitary waves (Alford et al. 2015).

Acknowledgements RC, RMM, and CT thank David Adalsteinsson for helpful comments on the post-processing of the numerical results using DataTank.

References

Alford MH, Peacock T, MacKinnon JA, Nash JD, Buijsman MC, Centuroni Luca R, Chao S-Y, Chang M-H, Farmer DM, Fringer OB (2015) The formation and fate of internal waves in the South China sea. Nature 521(7550):65–69

Almgren AS, Bell JB, Colella P, Howell LH, Welcome ML (1998) A conservative adaptive projection method for the variable density incompressible Navier-Stokes equations. J Comput Phys 142(1):1–46

Apel JR, Holbrook JR, Liu AK, Tsai JJ (1985) The Sulu sea internal soliton experiment. J Phys Oceanogr 15(12):1625–1651

Bell J, Berger M, Saltzman J, Welcome M (1994) Three-dimensional adaptive mesh refinement for hyperbolic conservation laws. SIAM J Sci Comput 15(1):127–138

Benjamin TB (1986) On the boussinesq model for two-dimensional wave motions in heterogeneous fluids. J Fluid Mech 165:445–474

Bourgault D, Galbraith PS, Chavanne C (2016) Generation of internal solitary waves by frontally forced intrusions in geophysical flows. Nat Commun 7:13606

Brandt P, Rubino A, Fischer J (2002) Large-amplitude internal solitary waves in the north equatorial countercurrent. J Phys Oceanogr 32(5):1567–1573

Camassa R, Tiron R (2011) Optimal two-layer approximation for continuously density stratification. J Fluid Mech 669:32–54

Camassa R, Viotti C (2012) On the response of large-amplitude internal waves to upstream disturbances. J Fluid Mech 702:59–88

Camassa R, Choi W, Michallet H, Rusås P-O, Seven JK (2006) On the realm of validity of strongly nonlinear asymptotic approximations for internal waves. J Fluid Mech 549:1–23

Carr M, Davies PA (2010) Boundary layer flow beneath an internal solitary wave of elevation. Phys Fluids 22(2):026601

Carr M, Fructus D, Grue J, Jensen A, Davies PA (2008) Convectively induced shear instability in large amplitude internal solitary waves. Phys Fluids 20(12):126601

Carr M, King SE, Dritschel DG (2011) Numerical simulation of shear-induced instabilities in internal solitary waves. J Fluid Mech 683:263–288

Carr M, Franklin J, King SE, Davies PA, Grue J, Dritschel DG (2017) The characteristics of billows generated by internal solitary waves. J Fluid Mech 812:541–577

Choi W, Camassa R (1996) Long internal waves of finite amplitude. Phys Rev Lett 77(9):1759

Choi W, Camassa R (1999) Fully nonlinear internal waves in a two-fluid system. J Fluid Mech 396:1–36

Churnside JH, Ostrovsky LA (2005) Lidar observation of a strongly nonlinear internal wave train in the Gulf of Alaska. Int J Remote Sens 26(1):167–177

Davis RE, Acrivos A (1967) Solitary internal waves in deep water. J Fluid Mech 29(3):593–607

Dong J, Zhao W, Chen H, Meng Z, Shi X, Tian J (2015) Asymmetry of internal waves and its effects on the ecological environment observed in the northern South China sea. Deep Sea Res 98:94–101

Dubreil-Jacotin M-L (1934) Part I: Sur la détermination rigoureuse des ondes permanentes périodiques d'ampleur finie. Part II: Suite de composition dans la théorie des groupes finis et abstraits et dans la théorie des idéaux de pôlynomes. Ph.D. thesis, École Normale Supérieur

Dubreil-Jacotin M-L (1933) Sur la détermination rigoureuse des ondes permanentes périodiques d'ampleur finie. Comptes Rendus Mathematique Academie des Sciences 197:818

Duda TF, Lynch JF, Irish JD, Beardsley RC, Ramp SR, Chiu C-S, Tang Tswen Y, Yang Y-J (2004) Internal tide and nonlinear internal wave behavior at the continental slope in the northern South China sea. IEEE J Ocean Eng 29(4):1105–1130

Dunphy M, Subich C, Stastna M (2011) Spectral methods for internal waves: indistinguishable density profiles and double-humped solitary waves. Nonlinear Proc Geophys 18(3):351–358

Fructus D, Carr M, Grue J, Jensen A, Davies PA (2009) Shear-induced breaking of large internal solitary waves. J Fluid Mech 620:1–29

Grimshaw R (1981) Slowly varying solitary waves in deep fluids. Proc R Soc A 376:319–332

Grimshaw R, Helfrich K (2012) The effect of rotation on internal solitary waves. IMA J Appl Math 77(3):326–339

Grimshaw R, Pelinovsky E, Talipova T (2003) Damping of large-amplitude solitary waves. Wave Motion 37(4):351–364

Grue J, Friis HA, Palm E, Rusås PO (1997) A method for computing unsteady fully nonlinear interfacial waves. J Fluid Mech 351:223–252

Grue J, Jensen A, Rusås P-O, Sveen JK (1999) Properties of large-amplitude internal waves. J Fluid Mech 380:257–278

Helfrich KR, Melville WK (2006) Long nonlinear internal waves. Annu Rev Fluid Mech 38:395–425

Hosegood P, van Haren H (2006) Sub-inertial modulation of semi-diurnal currents over the continental slope in the faeroe-shetland channel. Deep Sea Res 53(4):627–655

Huang X, Chen Z, Zhao W, Zhang Z, Zhou C, Yang Q, Tian J (2016) An extreme internal solitary wave event observed in the northern South China sea. Sci Rep 6:30041

Johnston TMS, Rudnick DL, Kelly SM (2015) Standing internal tides in the Tasman sea observed by gliders. J Phys Oceanogr 45(11):2715–2737

Kalisch H, Bona JL (2000) Models for internal waves in deep water. Discrete Contin Dyn Syst 6(1):1–20

Kodaira T, Waseda T, Miyata M, Choi W (2016) Internal solitary waves in a two-fluid system with a free surface. J Fluid Mech 804:201–223

Koop CG, Butler G (1981) An investigation of internal solitary waves in a two-fluid system. J Fluid Mech 112:225–251

Korteweg DJ, De Vries G (1895) On the change of form of long waves advancing in a rectangular canal, and on a new type of long stationary waves. Lond Edinb Dublin Philos Mag J Sci 39(240):422–443

Kubota T, Ko DRS, Dobbs LD (1978) Weakly-nonlinear, long internal gravity waves in stratified fluids of finite depth. AIAA J Hydronaut 12(4):157–165

Lamb KG (2014) Internal wave breaking and dissipation mechanisms on the continental slope/shelf. Ann Rev Fluid Mech 46:231–254

Lien R-C, DAsaro EA, Henyey F, Chang M-H, Tang T-Y, Yang Y-J (2012) Trapped core formation within a shoaling nonlinear internal wave. J Phys Oceanogr 42(4):511–525

Lien R-C, Henyey F, Ma B, Yang YJ (2014) Large-amplitude internal solitary waves observed in the northern South China sea: properties and energetics. J Phys Oceanogr 44(4):1095–1115

Liu AK, Holbrook JR, Apel JR (1985) Nonlinear internal wave evolution in the Sulu sea. J Phys Oceanogr 15(12):1613–1624

Liu AK, Ramp SR, Zhao Y, Tang TY (2004) A case study of internal solitary wave propagation during ASIAEX 2001. IEEE J Ocean Eng 29(4):1144–1156

Long RR (1953) Some aspects of the flow of stratified fluids: I. A theoretical investigation. Tellus 5(1):42–58

Luzzatto-Fegiz P, Helfrich KR (2014) Laboratory experiments and simulations for solitary internal waves with trapped cores. J Fluid Mech 757:354–380

Meunier P, Leweke T (2003) Analysis and treatment of errors due to high velocity gradients in particle image velocimetry. Exp Fluids 35(5):408–421

Michallet H, Barthélemy E (1998) Experimental study of interfacial solitary waves. J Fluid Mech 366:159–177

Moum JN, Farmer DM, Smyth WD, Armi L, Vagle S (2003) Structure and generation of turbulence at interfaces strained by internal solitary waves propagating shoreward over the continental shelf. J Phys Oceanogr 33(10):2093–2112

Passaggia P-Y, Leweke T, Ehrenstein U (2012) Transverse instability and low-frequency flapping in incompressible separated boundary layer flows: an experimental study. J Fluid Mech 703:363–373

Passaggia P-Y, Helfrich KR, White BL (2018) Optimal transient growth in thin-interface internal solitary waves. J Fluid Mech 840:342–378

Pinkel R (1979) Observations of strongly nonlinear internal motion in the open sea using a range-gated Doppler sonar. J Phys Oceanogr 9(4):675–686

Preusse M, Stastna M, Freistühler H, Peeters F (2012) Intrinsic breaking of internal solitary waves in a deep lake. PLoS One 7(7):e41674

Preusse M, Freistühler H, Peeters F (2012a) Seasonal variation of solitary wave properties in lake constance. J Geophys Res Oceans 117(C4)

Ramp SR, Tang TY, Duda TF, Lynch JF, Liu AK, Chiu C-S, Bahr FL, Kim H-R, Yang Y-J (2004) Internal solitons in the northeastern South China sea. Part I: sources and deep water propagation. IEEE. J Ocean Eng 29(4):1157–1181

Rudnick DL, Boyd TJ, Brainard RE, Carter GS, Egbert GD, Gregg MC, Holloway PE, Klymak JM, Kunze E, Lee CM (2003) From tides to mixing along the Hawaiian ridge. Science 301(5631):355–357

Sadek MM, Parras L, Diamessis PJ, Liu PL-F (2015) Two-dimensional instability of the bottom boundary layer under a solitary wave. Phys Fluids 27(4):044101

Simmons HL, Alford MH (2012) Simulating the long-range swell of internal waves generated by ocean storms. Oceanography 25(2):30–41

Stanton TP, Ostrovsky LA (1998) Observations of highly nonlinear internal solitons over the continental shelf. Geophys Res Lett 25:2695–2698

Stastna M, Lamb KG (2002) Large fully nonlinear internal solitary waves: the effect of background current. Phys Fluids 14(9):2987–2999

van Haren H (2013) Bottom-pressure observations of deep-sea internal hydrostatic and non-hydrostatic motions. J Fluid Mech 714:591–611

Vasiliy Vlasenko, Peter Brandt, Angelo Rubino (2000) Structure of large-amplitude internal solitary waves. J Phys Oceanogr 30(9):2172–2185

Xie J, He Y, Chen Z, Xu J, Cai S (2015) Simulations of internal solitary wave interactions with mesoscale eddies in the northeastern South China sea. J Phys Oceanogr 45(12):2959–2978

Zhang S, Alford MH (2015) Instabilities in nonlinear internal waves on the Washington continental shelf. J Geophys Res 120(7):5272–5283

Zhao BB, Ertekin RC, Duan WY, Webster WC (2016) New internal-wave model in a two-layer fluid. J Waterw Port Coast Ocean Eng 142:04015022